Compensating Anisotropy in Histological Serial Sections with Optical Flow-Based Interpolation

Oleg Lobachev
Visual Computing
University of Bayreuth
Bayreuth, Germany
oleg.lobachev@uni-bayreuth.de

Birte S. Steiniger
Anatomy and Cell Biology
Philipps-University of Marburg
Marburg, Germany
steinigb@staff.uni-marburg.de

Michael Guthe
Visual Computing
University of Bayreuth
Bayreuth, Germany
michael.guthe@uni-bayreuth.de

ABSTRACT

Histological serial sections allow for 3D representation of anatomical structures in microscopic to mesoscopic range. However, due to the nature of the acquisition, they suffer from severe anisotropy: 14-to-1 in a single average microscopic paraffin section. We present an interpolation method based on optical flow and show that standard interpolation methods are less suited for serial sections.

With our non-linear interpolation approach we are able to represent the "movement" of image parts that are of interest. This allows for better 3D reconstructions and further insights in microanatomy.

CCS CONCEPTS

• **Computing methodologies** → **Image processing**; *Tracking*; • **Applied computing** → **Imaging**;

KEYWORDS

interpolation, anisotropy, optical flow, histology, serial sections, medical imaging

ACM Reference Format:
Oleg Lobachev, Birte S. Steiniger, and Michael Guthe. 2017. Compensating Anisotropy in Histological Serial Sections with Optical Flow-Based Interpolation. In *SCCG '17: SCCG '17: Spring Conference on Computer Graphics 2017, May 15–17, 2017, Mikulov, Czech Republic.* ACM, New York, NY, USA, 11 pages. https://doi.org/10.1145/3154353.3154366

1 INTRODUCTION

Real world data, especially acquired from some special modalities like MRT or histology, often suffer from anisotropy. This means that in some dimensions the data are not sampled as frequently as in others. In other words, they feature rectangular, not square pixels or non-cubic voxels.

The most straightforward way to reduce or eliminate anisotropy is to interpolate the data forming a denser, ideally, uniform sampling grid. This paper discusses a *method* of interpolation that is more suitable for 3D reconstruction of histological data than standard approaches. Our approach maintains better connectivity of tissues across the sections despite small local spatial distortions.

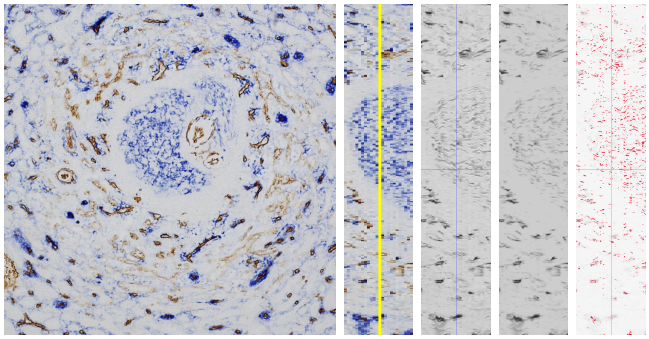

(a) Frontal plane of "spleen 2" (b) (c) (d) (e)

Figure 1: A quick summary of this paper. (a) shows the frontal plane of a volume obtained from histological serial sections, data set "spleen 2". (b), (c), and (d) show a z-profile of, correspondingly, registered data set, separated CD34-positive staining after interpolation, and final result of volume filtering. (e) highlights differences between unfiltered and filtered data. The focus of this paper is the interpolation (c) that facilitates better final meshes. The final rendering is in Figure 2.

Histology. Histology is an old medical investigation technique. Biological specimens are sectioned into thin layers ("sections"), color is added via "staining", a stained section can be inspected under a microscope. Improvements from using better cutting blades, motorized sectioning devices ("microtomes"), and immunohistology (most notable for us: monoclonal antibodies) allowed for more selective discrimination of varying cell types and more robust and stable sectioning. The advent of optical scanning microscopes allowed to acquire a whole section in a very high resolution and to deal with region selection and further processing later—and digitally. In this manner the microscopy session and image acquisition were reversed and detached from each other, the so-called "virtual microscopy" became viable. Further, scanning microscopes and overall advances in the sectioning and staining procedures allowed for "serial sections": not a single section is prepared, but a series of consecutive sections. With further processing (most notably: registration [Lobachev et al. 2017; Saalfeld et al. 2012; Sotiras et al. 2013]), a stack of serial sections can be treated as volume data. Such data are the starting point of this paper.

SCCG '17, May 15–17, 2017, Mikulov, Czech Republic

ACM ISBN 978-1-4503-5107-2/17/05…$15.00
https://doi.org/10.1145/3154353.3154366

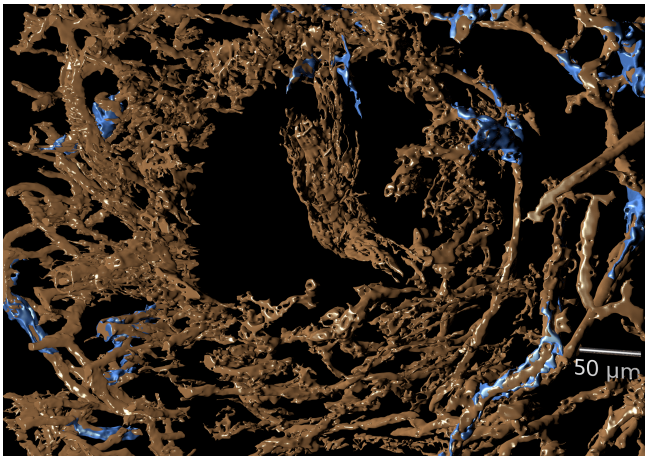

Figure 2: The final meshes for Fig. 1 for CD34-positive (brown) and CD271-positive cells (blue) in a rendering. The threshold for blue mesh generation was set rather high: the inside of the follicle is empty.

Multiple further medical imaging techniques exist, but no other is applicable in our setting. Non-invasive 3D imaging techniques like MRT or CT lack the resolution: modern scanning microscopes produce images at 0.25–0.3 µm/pixel in the xy plane for probes that easily reach 1 cm^2 area. Micro- and nano-CT methods either have orders of magnitude worse resolution or cannot deal with that large probes. We need to *stain* the specimen to see the cells of interest. We section the specimen for further processing and acquisition. However, sectioning of more than ≈ 30 µm of tissue is impractical for paraffin embeddings. An alternative might be fluorescence microscopy. In non-human probes it is even possible to genetically enhance cells with fluorescence, thus improving the separation of cell types. However, fluorescence labeling degrades very fast under illumination, while stainings for transmitted light microscopy are known to survive for decades. An interesting alternative is tissue clearing [Richardson and Lichtman 2015]: the refraction index of the tissue is adapted to the index of embedding fluid, but this approach is still highly experimental and has not been tried profoundly on human specimens and with transmitted light microscopy. Basically, for microanatomical research on human specimens no other technique except serial sectioning is practical and solidly established.

The huge drawback of serial sections is an anisotropy. While the resolution of a scanning microscope can reach 0.25 µm/pixel in the xy plane, the z axis is limited to the thickness of a section. The minimal thickness of sections in hard plastic embedding obtained with a conventional microtome may be 0.5 to 3 µm/section. The thickness of paraffin serial sections lies in the range of 5 to 8 µm/section. The maximal section thickness with paraffin embeddings and a conventional microtome can reach 25 to 30 µm. We aim for better 3D reconstructions from "conventional" serial sections. Our presentation in this paper focuses on serial sections with typical anisotropy 0.5 : 0.5 : 7 µm or 14-to-1. We reduce the anisotropy to 0.5 : 0.5 : 1 µm or 2-to-1. *Any* kind of serial section data would profit from our approach, actually, any kind of anisotropic data does.

2 RELATED WORK

Standard interpolation methods like bilinear interpolation, bicubic interpolation [Keys 1981], or Lanzos filter [Duchon 1979] (see also Burger and Burge [2009]) are of course related to this paper. However, we focus on a more special and non-generic use case: we would like to interpolate medical data in a way that improves subsequent 3D reconstruction. Our method uses optical flow.

2.1 Optical flow

Optical flow as such was defined by Horn and Schunck [1981], while Lucas and Kanade [1981] pioneered a viable way for computing it that is still used today. Baker et al. [2011] present a nice overview of optical flow methods and their evaluation. A lot of effort was invested into variants and improvements of optical flow [Brox et al. 2004; Brox and Malik 2011; Sun et al. 2010]. Recent improvements to the topic are presented by Revaud et al. [2015]. We use the *dense* optical flow computation [Farnebäck 2003]. Keeling and Ring [2005] use optical flow as a similarity metric for elastic image registration of medical images. It is in a sense dual to our approach: we also use optical flow as a measure for "movement" in two consecutive medical images. However, we use the detected motion to generate intermediates and not to decide what distortion needs to be applied to input images to make them more similar. Zitnick et al. [2005] combine image segmentation and optical flow computation.

2.2 Registration and 3D reconstruction of serial sections

An integrated suite for processing of serial sections is Track-EM2 [Cardona et al. 2010], a part of Fiji [Schindelin et al. 2012]. 3D reconstruction from serial sections is an increasingly popular topic [Gijtenbeek et al. 2005; Lobachev et al. 2017; Ma et al. 2008; Ourselin et al. 2001; Saalfeld et al. 2012; Steiniger et al. 2003, 2016; Xu et al. 2015]. It is especially of importance in the mesoscopic area which cannot be represented on with a single histological section. However, to align these sections, a *registration* method is needed. We used Lobachev et al. [2017] for fine-grain registration and Ulrich et al. [2014] for coarse-grain, slice-wide registration. Other approaches include elastic registration (e. g. Guest et al. [2001]), registration in feature space (e. g. Bağci and Bai [2008]), utilization of mutual information (e. g. Chappelow et al. [2011]; Rueckert et al. [1999]; Schnabel et al. [2001]), smoothness based registration [Cifor et al. 2011], thin-plate splines (e. g. Wan et al. [2013]).

2.3 Interpolation of medical data

Optical flow was used for interpolation in live MRT data to reduce breathing artifacts [Ehrhardt et al. 2007]. However, there are many differences. Ehrhardt et al. [2007] work on 4D MRT data, we operate on a set of 2D microscopic images. They apply a demons-based registration method similar to Thirion [1998], we directly apply the distortion field to (pre-registered) input images (Section 3). Ehrhardt et al. [2007] operate on $512 \times 512 \times 200 \times 10$ data (i. e. 5.24×10^8 voxels), but they report more than 30 hours run time. Our method

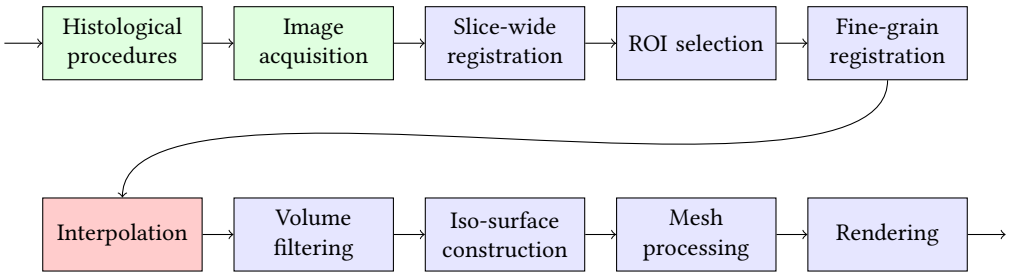

Figure 3: Our image processing pipeline. All steps after acquisition are digital. The focus of this paper is interpolation.

typically operates on 28.6–81.1% of their input volume, but produces results in a few minutes with a Python-based implementation. Decreased dimension helps in our case. Ehrhardt et al. [2007] use the method of Barron et al. [1994] for optical flow computation, we utilize the method of Farnebäck [2003]. We compare our approach to standard interpolation methods in Section 4.3.

Thevenaz et al. [2000] discuss in-depth the quality and applications of some existing and modified interpolation methods, it is mainly focused on choosing better basis functions. Lehmann et al. [1999] provide an overview of existing interpolation methods in context of medical imaging and aspect ratio correction.

3 METHOD

3.1 Synopsis of the pipeline

We process immunohistochemically stained serial sections (though the method is also applicable to other data), hence we outline our complete imaging pipeline in this section to facilitate better understanding of the actual method. Figure 3 shows the overall pipeline.

A removed and fixed specimen was embedded in paraffin [Steiniger et al. 2014a,b]. Bone marrow, however, was embedded into methylmethacrylate [Steiniger et al. 2013, 2016]. The specimens were sectioned on a microtome. The embedding medium was removed, and the sections were stained using several immunohistological methods. Then, images were acquired. Scans of the entire sections were performed using a transmitted light scanning microscope (Leica SCN 400). From this point on the processing was completely digital.

Entire sections (typically very large images, ranging at $20k$–$30k$ pixels per side) are coarsely registered [Ulrich et al. 2014]. This is needed for the subsequent selection of regions of interest (ROI). Potential irregularities in intensity caused by varying slice thickness are compensated with slice normalization [Khan et al. 2014; Reinhard et al. 2001]. The ROIs are finely registered [Lobachev et al. 2017], producing volume data. However, the anisotropy is severe. At this point the interpolation method presented here is used. After interpolation the volume can be further processed. We typically apply at least a closing filter and a minor Gaussian blur [Steiniger et al. 2016]. The filtered volume is used for mesh construction with marching cubes [Lorensen and Cline 1987]. The resulting mesh is post-processed. The actual processing depends on the objective, but it typically includes methods to close a few holes, to reduce the mesh size [Ju 2004], and to correctly smooth the surface [Taubin 1995]. The final mesh can be rendered with usual techniques.

We stress that our interpolation method allows for better meshes than standard approaches (Fig. 10 shows a comparison).

3.2 Dense optical flow

Farnebäck's dense optical flow [Farnebäck 2003] is defined in the following way. We aim to compare two signals, f_1 and f_2. They are modeled with quadric polynomials, e. g. $f_1(\mathbf{x}) = \mathbf{x}^T\mathbf{A}_1\mathbf{x} + \mathbf{b}_1^T\mathbf{x} + c_1$ for a symmetric matrix $\mathbf{A}_1$, a vector $\mathbf{b}_1$ and a scalar c_1. Assume f_2 is globally displaced by $\mathbf{d}$, it can be defined in a similar way in terms of $\mathbf{A}_2, \mathbf{b}_2$ and c_2. We can express $\mathbf{d}$ as $-\mathbf{A}_1^{-1}(\mathbf{b}_2 - \mathbf{b}_1)/2$. To make the computation more practical we use *local* polynomial approximations of images. In the following we omit the $\mathbf{x}$ argument, e. g. $\mathbf{A}$ always stands for a local approximation $\mathbf{A}(\mathbf{x})$. Let

$$\mathbf{A} := (\mathbf{A}_1 + \mathbf{A}_2)/2 \quad \text{and} \quad \Delta\mathbf{b} := -(\mathbf{b}_2 - \mathbf{b}_1)/2.$$

The distance is now a spatially varying displacement field $\mathbf{d}$ with $\mathbf{A}\mathbf{d} = \Delta\mathbf{b}$. With a weight function w—the edges of an image have a smaller weight—in a neighborhood I holds:

$$\mathbf{d}(\mathbf{x}) = \sum_I w\mathbf{A}^T\Delta\mathbf{b} \Big/ \sum_I w\mathbf{A}^T\mathbf{A}, \tag{1}$$

the sums run over all $\mathbf{x}$ in I, as $\mathbf{x}$ is an omitted for brevity argument to $\mathbf{A}$, $\Delta\mathbf{b}$, and w. In practice we compute $\mathbf{A}^T\mathbf{A}$, $\mathbf{A}^T\Delta\mathbf{b}$, and $\Delta\mathbf{b}^T\Delta\mathbf{b}$ (needed for the confidence value) pointwise.

The flow is computed on multiple scales to alleviate the problem with larger displacements. We compute the flow based on a classical 2^n image pyramid with 3 levels, averaging window size of 15 pixels, three iterations at each level, neighborhood size for polynomial expansion of 5 pixels. The derivatives for polynomial expansion are smoothed with $\sigma = 1.2$.

Let us denote with $\mathcal{D}(\mathbf{A}, \mathbf{B})$ the complete computation of dense optical flow between $\mathbf{A}$ and $\mathbf{B}$. It is basically a vector field that consists of local approximations $\mathbf{d}(\mathbf{x})$. Currently, we compute it with Open CV [Bradski and Kaehler 2008] function calcOpticalFlowFarneback.

3.3 Computing the interpolations

Now let $\mathcal{F}_{\mathbf{A},\mathbf{B}}(r, \cdot)$ be the distortion operator of dense optical flow between images $\mathbf{A}$ and $\mathbf{B}$. Here is $0 \le r \le 1$ the magnitude of the flow. The operator $\mathcal{F}_{\mathbf{A},\mathbf{B}}(r, \mathbf{X})$ computes the optical flow $\mathcal{D}$ and spatially displaces the input image $\mathbf{X}$ by $r\mathcal{D}(\mathbf{A}, \mathbf{B})$. The displacement is applied to the input image with Open CV remap function. In most cases, however, $\mathbf{X}$ is either $\mathbf{A}$ or $\mathbf{B}$. Basically, $\mathcal{F}_{\mathbf{A},\mathbf{B}}(1/2, \mathbf{A})$ distorts $\mathbf{A}$ to correspond to the optical flow from $\mathbf{A}$ to $\mathbf{B}$ at a half magnitude.

Naturally, $\mathcal{F}_{\mathbf{A},\mathbf{B}}(0,\mathbf{A}) = \mathbf{A}$ and $\mathcal{F}_{\mathbf{B},\mathbf{A}}(0,\mathbf{B}) = \mathbf{B}$. However, $\mathcal{F}_{\mathbf{A},\mathbf{B}}(1,\mathbf{A})$ is not **B**, but **A**, distorted in a way to be similar to **B**. We compute a sequence of $n+1$ images $\mathbf{I}_k$, $0 \le k \le n$ as

$$\mathbf{I}_k = \frac{k}{n}\mathcal{F}_{\mathbf{A},\mathbf{B}}\left(\frac{k}{n},\mathbf{A}\right) + \frac{n-k}{n}\mathcal{F}_{\mathbf{B},\mathbf{A}}\left(\frac{n-k}{n},\mathbf{B}\right). \quad (2)$$

Figure 4 illustrates this process. In our particular application we compute intermediate images such that the anisotropy is no more 0.5 : 0.5 : 7 µm, but merely 0.5 : 0.5 : 1 µm. All figures showing our method in this paper (except parts of Figure 4) feature images $\mathbf{I}_k$.

Pseudo code. Figure 5 details on our method in pseudo code. We compute the optical flow twice. Notice that due to different displacement representations in calcOpticalFlowFarneback and remap, the optical flows D_1 and D_2 need to be converted to another representation, the x- and y-maps. This operation is, however, trivial at large. Only after the conversion the flow can be scaled. To summarize: we gradually apply the dense optical flow to input images, blending the results to final images $\mathbf{I}_k$.

4 RESULTS

First we present the specimens to which we apply our method. Then we showcase how our optical flow-based interpolation improves 3D reconstruction. Finally, we compare our method to the state of the art.

4.1 Specimens and the processing pipeline

We report our finding based on multiple data sets. The specimens are listed in Table 1. All specimens are human and have been stained for transmitted light microscopy:

- Spleen, single staining: 24 serial sections, immunostained for the glycoprotein CD34 (brown), thus showing primarily capillary walls. Data were acquired by VMscope GmbH with a scanning microscope at 0.3 µm/pixel resolution. The current ROI was resized during processing. The specimen is called here "spleen 1".
- Spleen, double staining: same specimen as above (24 serial sections), additionally stained for CD271 (violet-blue) after first acquisition. It shows primarily capillaries (brown) and special structures called "capillary sheaths" (violet-blue). Data were acquired using a Canon 60D camera on a Zeiss Axiophot microscope. We refer to these data as "spleen 2".
- Spleen, double staining: 24 serial sections, immunostained for the glycoprotein CD34, smooth muscle cells (both brown), and for CD271 (violet-blue). This staining shows primarily capillaries, capillary sheaths, and smooth muscle alpha actin (SMA, targeted with asm-1) in the walls of larger blood vessels, such as arteries and arterioles [Steiniger et al. 2014a,b]. The interior of follicles is also weakly stained in blue. We call these data "spleen 3".
- Bone marrow: 21 serial sections, sectioned using a hard plastic embedding technique [Steiniger et al. 2013], immunostained for the glycoproteins CD34 and CD141 (both brown) [Steiniger et al. 2016], thus visualizing microvessels (both capillaries and sinuses) and larger blood vessels. We refer to these data as "bone marrow".

Table 1: Medical data sets used. All specimens are human. Resolution is stated in µm/pixel.

Organ	Antigen	Stain color	Resolution	Fig.
Spleen 1	CD34	brown	0.6	6
Spleen 2	CD34 CD271	brown violet-blue	0.416	1, 2
Spleen 3	CD34 SMA CD271	brown brown violet-blue	0.5	9–12
Bone marrow	CD34 CD141	brown brown	0.5	4, 8
Tonsil	CD38 SMA	brown brown	0.208	7

- Tonsil pilot experiment: 5 consecutive sections at 4 µm, immunostained for glycoprotein CD38 and SMA (both brown). Data were acquired using a Canon 60D camera on a Zeiss Axiophot microscope. We refer to these data here as "tonsil".

Large images (all except "spleen 2" and "tonsil") were pre-registered using a whole-slice registration method [Ulrich et al. 2014], then regions of interest (ROI) were selected. These regions were registered again using a fine-grain registration [Lobachev et al. 2017]. The "spleen 2" data set was aligned to a pre-selected ROI and finely registered with the same method. The data set "tonsil" was registered using a rigid-only method. For further processing a single channel was selected to yield grayscale images. Then anisotropy was reduced with interpolation, the actual focus of this paper. Further processing was done with 3D Slicer [Fedorov et al. 2012]. We used Fiji to produce z-stacks and as a reference implementation for standard interpolation methods.

4.2 Interpolation and 3D reconstruction

Figure 1 shows the "spleen 2" data set evolving from registered serial sections to final rendering. The z-profiles of the input stack and interpolated brown staining (after segmentation) showcase our method (Figure 1, (b) and (c)). The volume filtering after interpolation is subtle (d), but it makes some difference, as shown by a PSNR difference image at 5% threshold (e) shows. Figure 2 demonstrates the final rendering of both brown (CD34, capillary walls) and violet-blue (CD271, capillary sheaths) stainings, interpolated with our method. The weaker staining of some blood vessels outside of the follicle in Figure 1 is deliberate. It represents further blood vessel types, irrelevant for present investigation. Only structures that are very intensively stained in blue are represented in Fig. 2, this corresponds to capillary sheaths.

Figs. 6 and 7 show "spleen 1" and "tonsil" data sets respectively. The anisotropy is reduced using an interpolation with our method. Border effects are present in Fig. 6. This could be avoided when the interpolation would be performed on a slightly larger data set that would be consequently cropped down.

Figure 10 shows the reconstructed meshes from the same input data set "spleen 3", but for varying interpolation methods. We omit

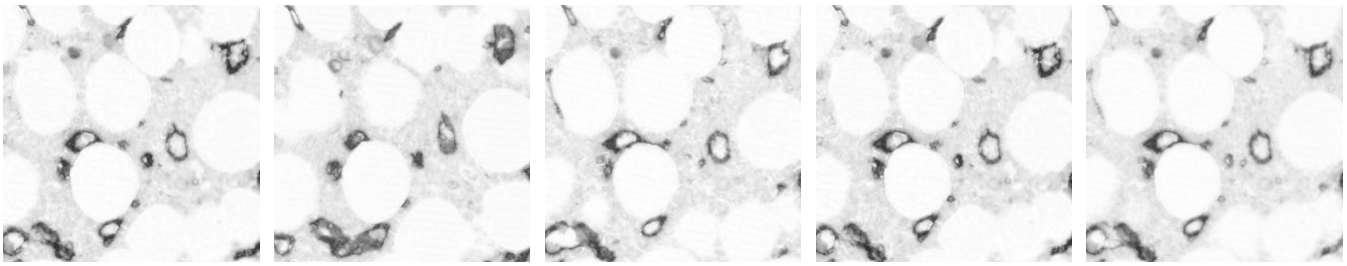

(a) First image, A (b) Second image, B (c) Interpolation from A to B (d) Interpolation from B to A (e) Final result, sum of both interpolations

Figure 4: Illustrating interpolation with dense optical flow on "bone marrow" data set [Steiniger et al. 2016], HSV saturation channel, negative image shown. We interpolate with $n = 7$, showing images for $k = 3$. From left to right: first and second input images, A (a) and B (b), interpolation from A to B (c), i. e. $\mathcal{F}_{\mathrm{A},\mathrm{B}}(3/7, \mathrm{A})$, interpolation from B to A (d) , i. e. $\mathcal{F}_{\mathrm{B},\mathrm{A}}(3/7, \mathrm{B})$, the final result, i. e. the image I_3 (e). Scale bar is 100 µm.

1. $\mathbf{A} \leftarrow$ read image 1, $\mathbf{B} \leftarrow$ read image 2
2. compute $D_1 = \mathcal{D}(\mathbf{A}, \mathbf{B})$ and $D_2 = \mathcal{D}(\mathbf{B}, \mathbf{A})$ (using calcOpticalFlowFarneback)
3. **for** $k \in \{0, \ldots, n\}$ **do**
4. $\quad D_1^{(k)} \leftarrow$ scale D_1 with factor k/n
5. $\quad D_2^{(k)} \leftarrow$ scale D_2 with factor $(n-k)/n$
6. $\quad$ compute $\mathcal{F}_{\mathbf{A},\mathbf{B}}(k/n, \mathbf{A})$: apply the map $D_1^{(k)}$ to image $\mathbf{A}$ with remap, yielding $\mathbf{A}^{(k)}$
7. $\quad$ compute $\mathcal{F}_{\mathbf{B},\mathbf{A}}((n-k)/n, \mathbf{B})$: apply the map $D_2^{(k)}$ to image $\mathbf{B}$ with remap, yielding $\mathbf{B}^{(k)}$
8. $\quad \mathbf{I}_k \leftarrow$ alpha-blend $\mathbf{A}^{(k)}$ and $\mathbf{B}^{(k)}$ with weights k/n and $(n-k)/n$
9. $\quad$ write image $\mathbf{I}_k$.

Figure 5: Pseudo code for our method.

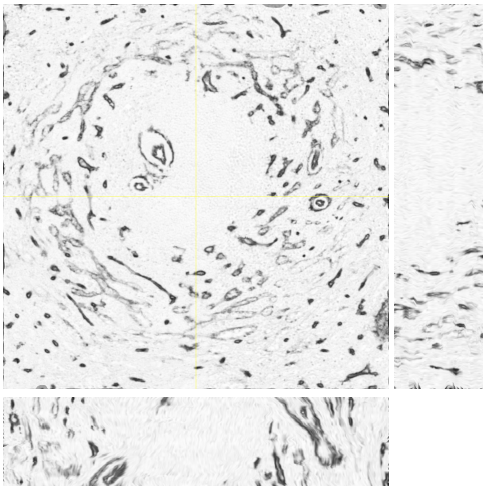

Figure 6: Interpolation with our method for "spleen 1". We interpolated across 24 serial sections.

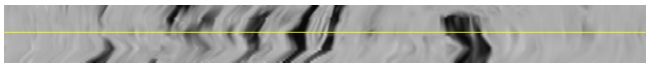

Figure 7: A z-profile after interpolation of "tonsil" data set with our method. The data was generated from 5 initial sections.

all volume and mesh filtering (aside from mesh repair [Ju 2004]) for the demonstration purpose. Figure 10b shows the final result with our method and all the filtering. Notice that the blood vessel in the foreground features a discontinuity with all methods used, but not with ours. This is due to the optical flow-based interpolation. Our registration method undistorts the sections and aligns them to each other. Nevertheless microvessels may shift for more than the diameter of small capillaries in the input images. This may happen because of artifacts or registration errors. Through "shifts" in the flow our method avoids discontinuities, but introduces additional waviness. Our method also features more constant intensity values in intermediate images. A further reason for discontinuities of microscopic blood vessels in other methods is *blending*. Varying intensity in bilinear or bicubic interpolation produces images more pleasant to the eyes, but tightly chosen iso-values in mesh construction yield holes where two structures are blended over (Fig. 9).

Bone marrow reconstruction is shown in Fig. 8, a detail showing intermediate phases of the interpolation is in Figure 4. Fig. 8a shows an overview. Fig. 8b shows a computation of shape diameter function on the reconstructed mesh. This computation allows experts to distinguish capillaries from sinus blood vessels [Steiniger et al. 2016].

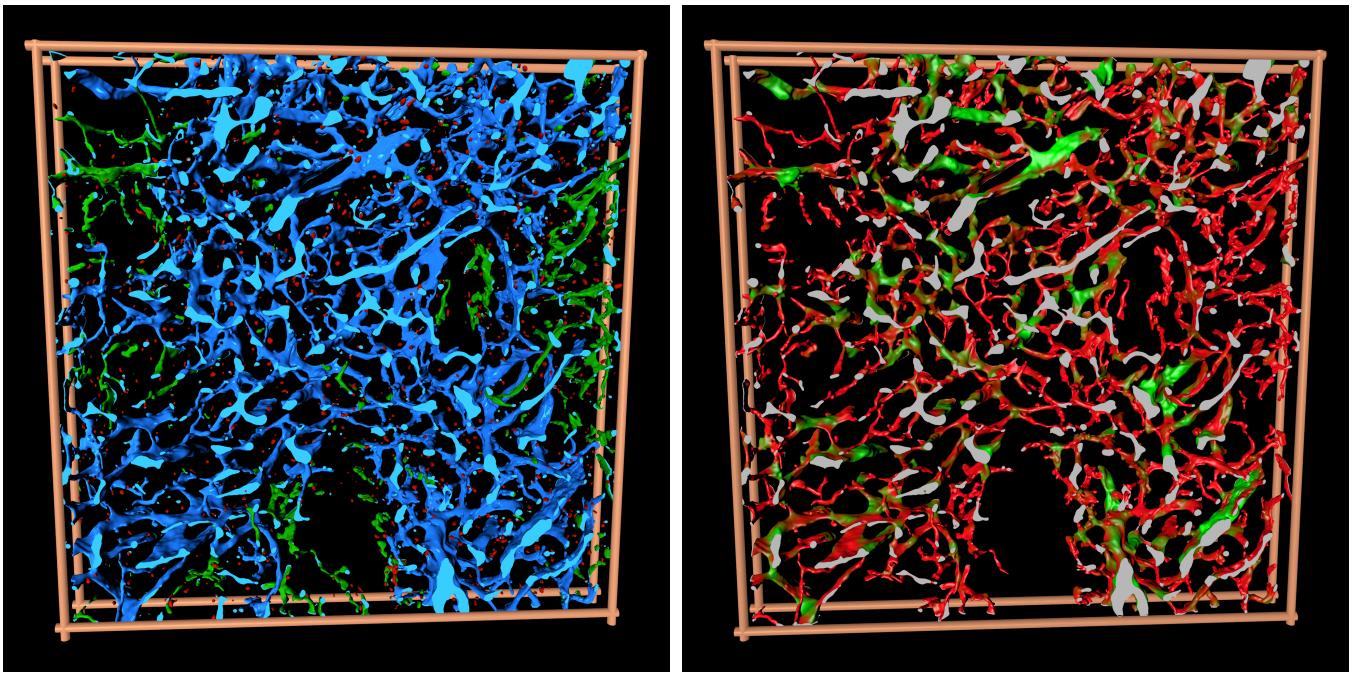

(a) Overview (b) Shape diameter function

Figure 8: 3D reconstruction of a "bone marrow" specimen. The anisotropy was reduced with our method. (a): overview, (b): cleaned-up mesh with computation of the shape diameter function that helped to discriminate blood vessel types [Steiniger et al. 2016].

4.3 Comparing with the state of the art

We compare our method to nearest neighbor interpolation and to bicubic interpolation with Fiji [Schindelin et al. 2012] in Figures 9–12.

The main attribute of our method is that two spatially close, but not necessarily overlapping objects on two consecutive sections are "morphed" into each other and not "blended", i. e. are not "faded out" from one object while "faded in" to another. The latter is typical of interpolation, but results in smaller intensities during "blending" that contribute to discontinuities in reconstructed meshes (Fig. 10). We *do* use alpha-blending in our computation, but the "fading" effect is much less with our method. For our medical application retained connectivity is more important than minor shape changes. This behavior is visible in Fig. 12.

Figure 9 shows all intermediate images between two consecutive frames, bicubicly interpolated and generated with our method. The effect of our method is even more visible in the Supplementary Video.

4.4 Application to generic data

To showcase that our method is applicable not only in medical imaging, we applied our method to images from USC-SIPI image database. We utilized the images "moon" (5.1.09, upscaled to 512 × 512 pixels, Fig. 13) and "bridge" (5.2.10, Fig. 14). In both cases we applied different distortions to the original image, yielding two input images. Then we generated 12 interpolations between these distorted images with our method. Figure 14 shows multiple output images $\mathbf{I}_k$ from our method along with the original image and input data. Here, we have cropped the images to the center to reduce border effects. We also crop after interpolation in the production use of our method in medical imaging. We deem the results of our method on test images as usable. Thus our method is applicable not only to medical images.

5 CONCLUSIONS AND FUTURE WORK

We present a special non-linear interpolation method to compensate anisotropy in histological serial sections. Using dense optical flow we determine the "movement" in the consecutive images. This movement is then gradually applied, generating intermediate images. This way our method retains more connectivity in the final meshes than standard interpolation methods. The benefit of our method consists in less intensity changes in interpolated images, and thus less danger that marching cubes algorithms interpret decreasing intensity as a discontinuity.

Our method has been applied to serial sections of specimens from varying human organs. It facilitated advances in fundamental medical research concerning bone marrow microvasculature [Steiniger et al. 2016]. Our method allowed to improve 3D representations, leading to new insights in microanatomy.

As we pre-register the data anyway, it is possible to retain the distortions from non-rigid registration phase. One might use these data and not dense optical flow for interpolation. In any case, it

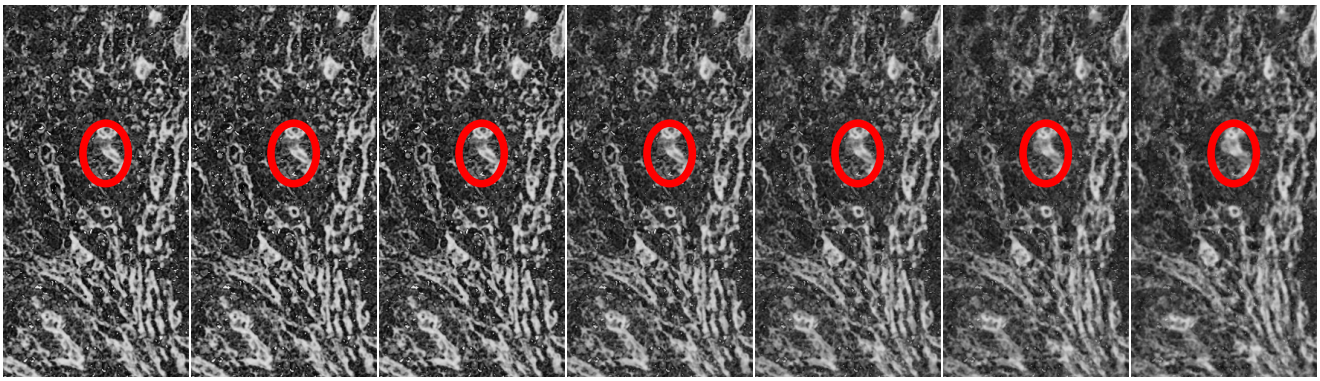

(a) Bicubic interpolation, crop

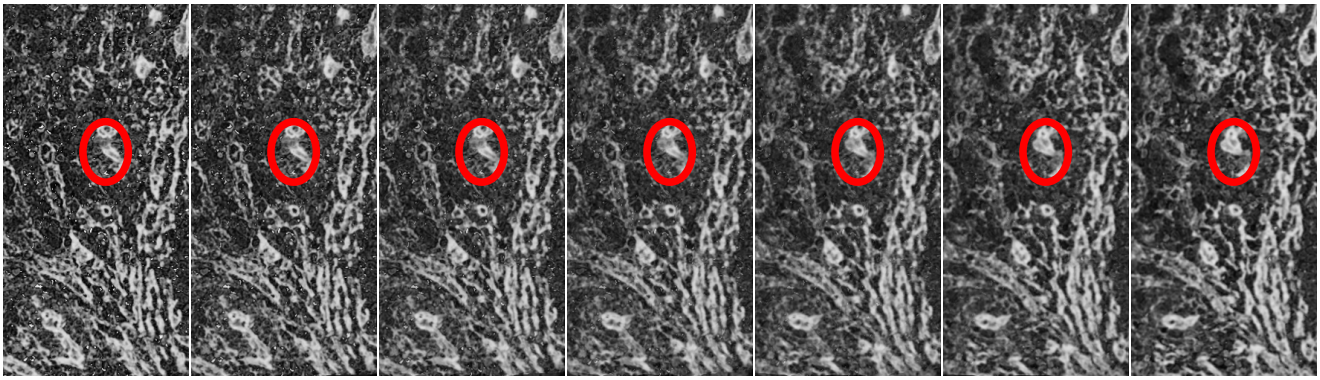

(b) Our method, crop

Figure 9: Interpolation sequence between two consecutive slices of "spleen 3", a 250×500 crop from center. (a): bicubic interpolation, (b): our method, $n = 6$. Observe the movement in the marked area. Supplementary Video shows the effect of our method in motion.

would make sense to generalize the distortion data to more than two images and to use e. g. spline-based interpolation. Applications of our method to serial sections from further organs and to data acquired from other modalities (e. g. electron microscopy or MRT) are, of course, possible.

ACKNOWLEDGMENTS

The authors would like to thank Anja Seiler, Katrin Lampp, and Verena Wilhelmi from the Institute of Anatomy and Cell Biology of Philipps-University of Marburg for producing the sections and performing the immunostaining. In addition, we thank Sandra Iden, Nikolay Kladt, and Astrid Schauss from the CECAD Cluster of Excellence at the University of Cologne and Verena Wilhelmi for helping with image acquisition. Vitus Stachniss from Restorative Dentistry and Endodontics of Philipps-University of Marburg contributed a lot to establish methylmethacrylate embedding technique. We thank the anonymous reviewers for their insightful comments that helped to improve this paper.

REFERENCES

Simon Baker, Daniel Scharstein, J. P. Lewis, Stefan Roth, Michael J. Black, and Richard Szeliski. 2011. A Database and Evaluation Methodology for Optical Flow. *International Journal of Computer Vision* 92, 1 (2011), 1–31. https://doi.org/10.1007/s11263-010-0390-2

J. L. Barron, D. J. Fleet, and S. S. Beauchemin. 1994. Performance of optical flow techniques. *International Journal of Computer Vision* 12, 1 (1994), 43–77. https://doi.org/10.1007/BF01420984

U. Bağci and L. Bai. 2008. Registration of standardized histological images in feature space. In *Proc. SPIE*, Vol. 6914. https://doi.org/10.1117/12.770219

Gary Bradski and Adrian Kaehler. 2008. *Learning OpenCV: Computer vision with the OpenCV library.* O'Reilly.

T. Brox, A. Bruhn, N. Papenberg, and J. Weickert. 2004. High accuracy optical flow estimation based on a theory for warping. In *European Conference on Computer Vision (ECCV) (LNCS 3024).* Springer, 25–36. http://lmb.informatik.uni-freiburg.de//Publications/2004/Bro04a

T. Brox and J. Malik. 2011. Large Displacement Optical Flow: Descriptor Matching in Variational Motion Estimation. *IEEE Transactions on Pattern Analysis and Machine Intelligence* 33, 3 (2011), 500–13. https://doi.org/10.1109/TPAMI.2010.143

Wilhelm Burger and Mark James Burge. 2009. *Principles of digital image processing.* Springer.

Albert Cardona, Stephan Saalfeld, Stephan Preibisch, Benjamin Schmid, Anchi Cheng, Jim Pulokas, Pavel Tomancak, and Volker Hartenstein. 2010. An Integrated Micro- and Macroarchitectural Analysis of the Drosophila Brain by Computer-Assisted Serial Section Electron Microscopy. *PLOS Biology* 8, 10 (10 2010), 1–17. https://doi.org/10.1371/journal.pbio.1000502

Jonathan Chappelow, B. Nicolas Bloch, Neil Rofsky, Elizabeth Genega, Robert Lenkinski, William DeWolf, and Anant Madabhushi. 2011. Elastic registration of multimodal

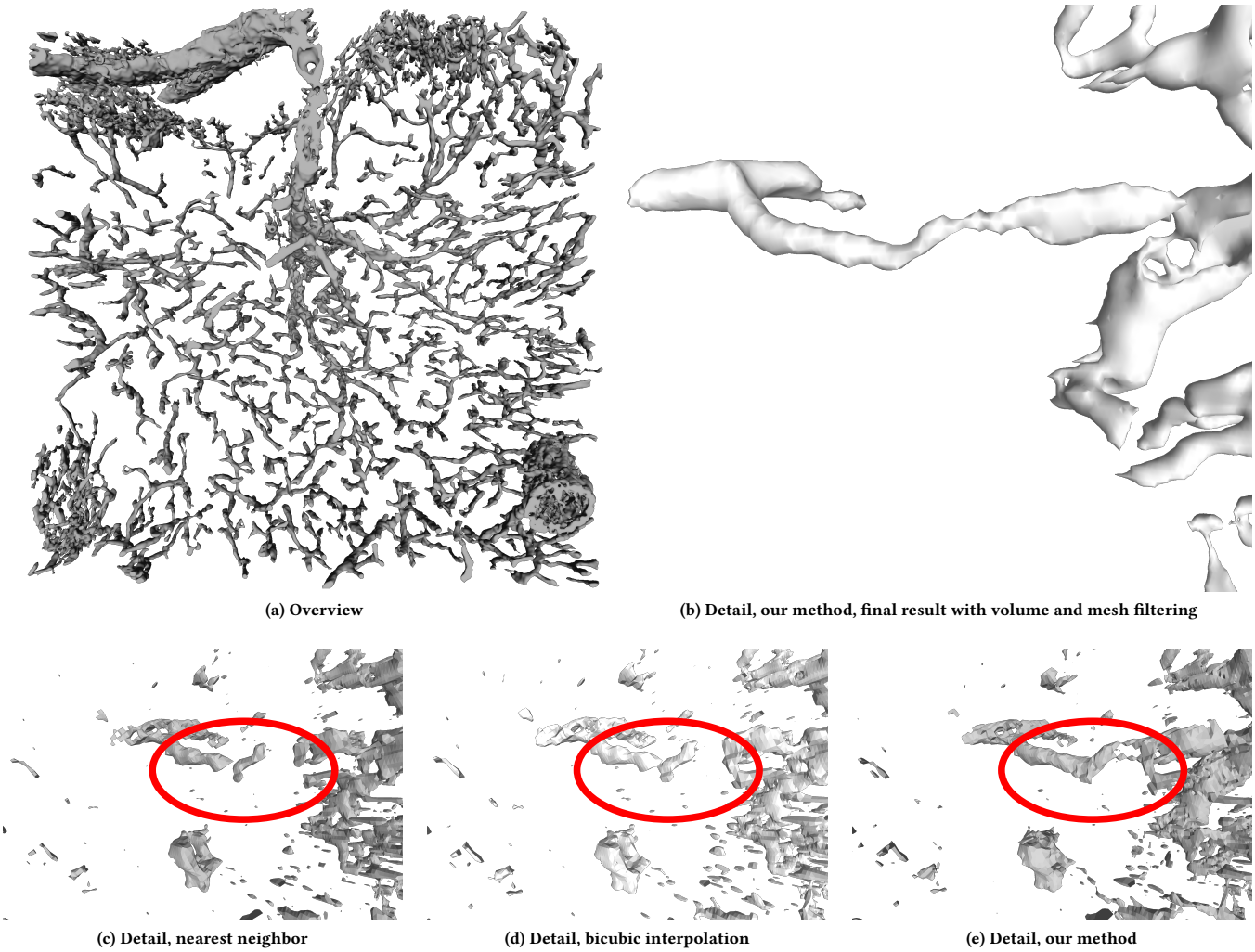

(a) Overview

(b) Detail, our method, final result with volume and mesh filtering

(c) Detail, nearest neighbor

(d) Detail, bicubic interpolation

(e) Detail, our method

Figure 10: 3D reconstructions of the same "spleen 3" data set after varying interpolation methods. To put more emphasis on interpolation, we used no volume filtering and only mesh healing with PolyMender [Ju 2004] in (c)–(e), while (b) shows the final result of our pipeline. Notice the discontinuity of blood vessel in (c)–(d), it is avoided in our method (b), (e).

prostate MRI and histology via multiattribute combined mutual information. *Med. Phys.* 38, 4 (2011), 2005–18. https://doi.org/10.1118/1.3560879

Amalia Cifor, Li Bai, and Alain Pitiot. 2011. Smoothness-guided 3-D reconstruction of 2-D histological images. *NeuroImage* 56, 1 (2011), 197–211. https://doi.org/10.1016/j.neuroimage.2011.01.060

Claude E Duchon. 1979. Lanczos filtering in one and two dimensions. *Journal of Applied Meteorology* 18, 8 (1979), 1016–22.

Jan Ehrhardt, René Werner, Dennis Säring, Thorsten Frenzel, Wei Lu, Daniel Low, and Heinz Handels. 2007. An optical flow based method for improved reconstruction of 4D CT data sets acquired during free breathing. *Medical Physics* 34, 2 (2007), 711–21. https://doi.org/10.1118/1.2431245

Gunnar Farnebäck. 2003. Two-Frame Motion Estimation Based on Polynomial Expansion. In *Image Analysis*, Josef Bigun and Tomas Gustavsson (Eds.). 363–70. https://doi.org/10.1007/3-540-45103-X_50

Andriy Fedorov, Reinhard Beichel, Jayashree Kalpathy-Cramer, Julien Finet, Jean-Christophe Fillion-Robin, Sonia Pujol, Christian Bauer, Dominique Jennings, Fiona Fennessy, Milan Sonka, et al. 2012. 3D Slicer as an image computing platform for the Quantitative Imaging Network. *Magn. Reson. Imaging* 30, 9 (2012), 1323–41.

J. M. Gijtenbeek, P. Wesseling, C. Maass, L. Burgers, and J. A. van der Laak. 2005. Three-dimensional reconstruction of tumor microvasculature: simultaneous visualization of multiple components in paraffin-embedded tissue. *Angiogenesis* 8, 4 (2005), 297–305.

E. Guest, E. Berry, R.A. Baldock, M. Fidrich, and M.A. Smith. 2001. Robust point correspondence applied to two- and three-dimensional image registration. *IEEE T. Pattern Anal. Mach. Intell.* 23, 2 (2001), 165–79. https://doi.org/10.1109/34.908967

Berthold K.P. Horn and Brian G. Schunck. 1981. Determining optical flow. *Artificial Intelligence* 17, 1 (1981), 185–203. https://doi.org/10.1016/0004-3702(81)90024-2

Tao Ju. 2004. Robust repair of polygonal models. *ACM T. Graphic.* 23, 3 (2004), 888–95.

Stephen L. Keeling and Wolfgang Ring. 2005. Medical Image Registration and Interpolation by Optical Flow with Maximal Rigidity. *Journal of Mathematical Imaging and Vision* 23, 1 (2005), 47–65. https://doi.org/10.1007/s10851-005-4967-2

R. Keys. 1981. Cubic convolution interpolation for digital image processing. *IEEE Transactions on Acoustics, Speech, and Signal Processing* 29, 6 (1981), 1153–60. https://doi.org/10.1109/TASSP.1981.1163711

A. M. Khan, N. Rajpoot, D. Treanor, and D. Magee. 2014. A Nonlinear Mapping Approach to Stain Normalization in Digital Histopathology Images Using Image-Specific Color Deconvolution. *IEEE T. Biomed. Eng.* 61, 6 (2014), 1729–38. https://doi.org/10.1109/TBME.2014.2303294

T. M. Lehmann, C. Gonner, and K. Spitzer. 1999. Survey: interpolation methods in medical image processing. *IEEE T. Med. Imaging* 18, 11 (1999), 1049–75. https://doi.org/10.1109/42.816070

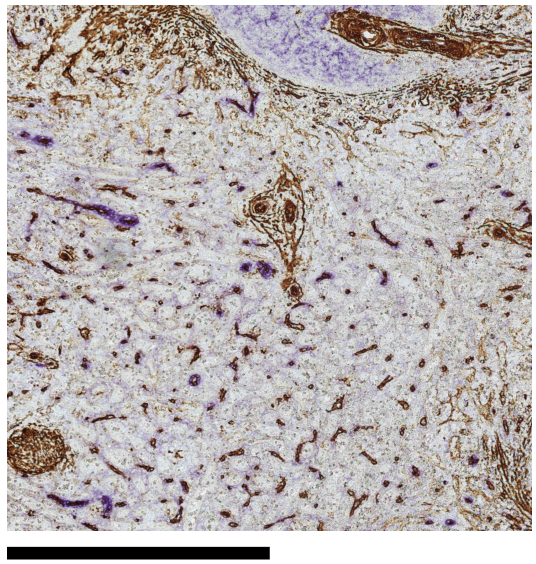

(a) Original data, slice 11 of 24

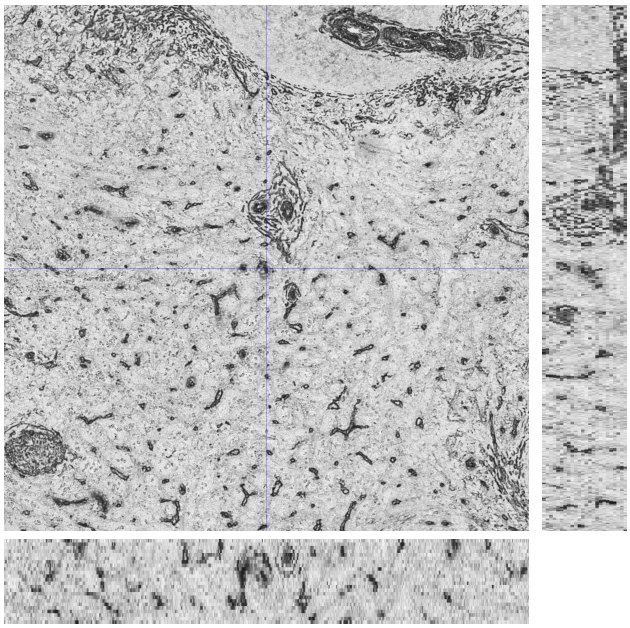

(b) Nearest neighbor

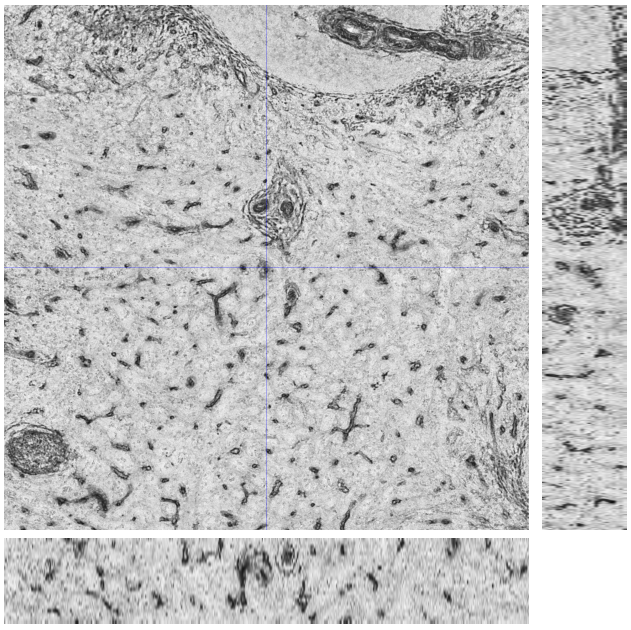

(c) Bicubic interpolation

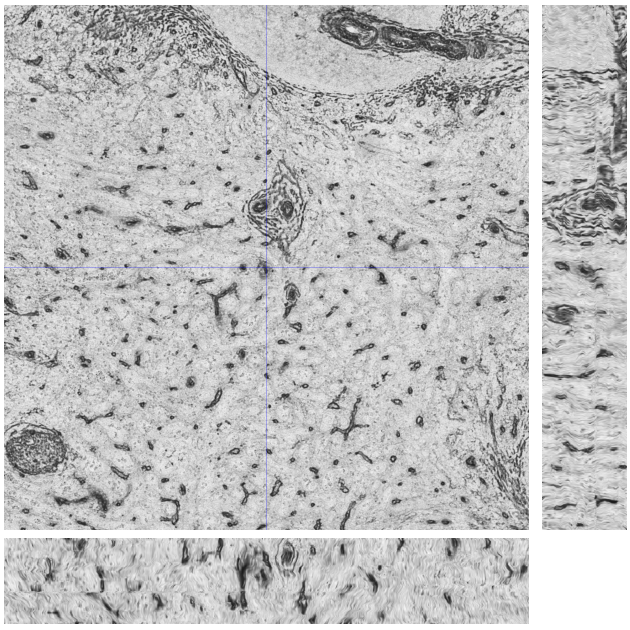

(d) Our method

Figure 11: Comparing various interpolation methods for a "spleen 3" data set, size $2k \times 2k$ pixels, 24 initial sections. All interpolation methods (b)–(b) operate on CMYK karbon channel of original data (a). We show the center of the 24 slice data set, the z-profiles are also cut in the center of the data set, at $1k$ pixels. We show the negative of the interpolated data. Notice that though our method (d) produces some "waviness", interpolated data keep similar intensity for varying spatial positions. This is not the case with usual interpolation methods (b), (c). Scale bar = 500 µm.

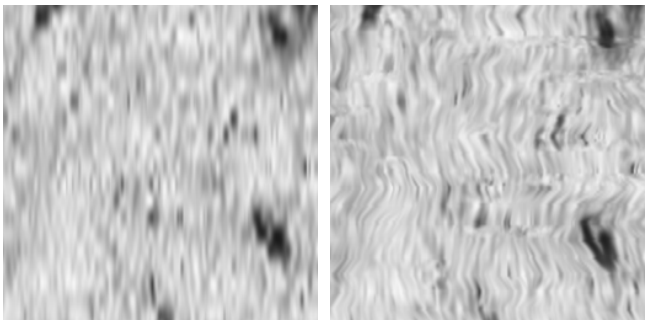

(a) Bicubic interpolation (b) Our method

Figure 12: Crops from xz-plane stacks from Figure 11 at a larger magnification. Bicubic interpolation (a) does not connect slightly misaligned dark blobs (we assume these are capillaries). Our method (b) is able to do so, but produces some waviness.

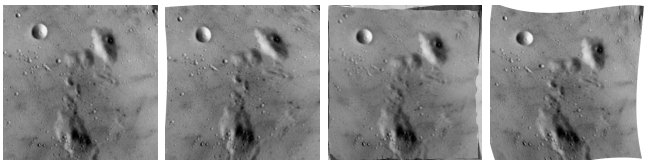

(a) (b) A, $k = 0$ (c) $k = 6$ (d) B, $k = 12$

Figure 13: Our method on distorted "moon" images. We show full images, notice the border effects. (a) Upscaled original image. (b) First input image. (c) Interpolation result, image from the middle of the interpolation stack. (d) Second input image.

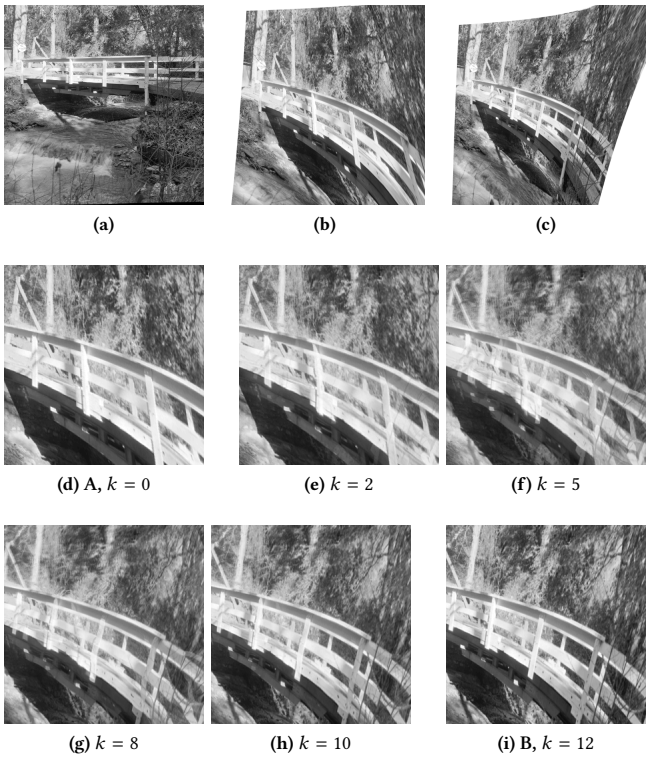

(a) (b) (c)

(d) A, $k = 0$ (e) $k = 2$ (f) $k = 5$

(g) $k = 8$ (h) $k = 10$ (i) B, $k = 12$

Figure 14: Our method on distorted "bridge" images. Top row shows the original image and both distorted input images. Middle and bottom rows show the cropped input images for reference and the in-between images generated with our method. (a) shows original image, (b) is the full first input image, (c) is the full second input image; (d) is the cropped first input image A; (e)–(h) are the interpolated images, $k = 2, 5, 8, 10$ respectively, $n = 12$; (i) is the cropped second input image B.

O. Lobachev, Ch. Ulrich, B. S. Steiniger, V. Wilhelmi, V. Stachniss, and M. Guthe. 2017. Feature-based multi-resolution registration of immunostained serial sections. *Med. Image Anal.* 35 (2017), 288–302. https://doi.org/10.1016/j.media.2016.07.010

William E. Lorensen and Harvey E. Cline. 1987. Marching cubes: A high resolution 3D surface construction algorithm. *Comput. Graph. (ACM)* 21, 4 (1987), 163–9. https://doi.org/10.1145/37402.37422

Bruce D Lucas and Takeo Kanade. 1981. An iterative image registration technique with an application to stereo vision.. In *International Joint Conference on Artificial Intelligence (IJCAI '81)*. 674–9.

Bin Ma, Lei Wang, Reinhard von Wasielewski, Werner Lindenmaier, and Kurt E. J. Dittmar. 2008. Serial sectioning and three-dimensional reconstruction of mouse Peyer's patch. *Micron* 39, 7 (2008), 967–75. https://doi.org/10.1016/j.micron.2007.10.007

S. Ourselin, A. Roche, G. Subsol, X. Pennec, and N. Ayache. 2001. Reconstructing a 3D structure from serial histological sections. *Image & Vision Comput.* 19 (2001), 25–31. Issue 1–2. https://doi.org/10.1016/S0262-8856(00)00052-4

E. Reinhard, M. Adhikhmin, B. Gooch, and P. Shirley. 2001. Color transfer between images. *IEEE Comput. Graph.* 21, 5 (2001), 34–41. https://doi.org/10.1109/38.946629

Jerome Revaud, Philippe Weinzaepfel, Zaid Harchaoui, and Cordelia Schmid. 2015. EpicFlow: Edge-Preserving Interpolation of Correspondences for Optical Flow. In *Computer Vision and Pattern Recognition*. 1164–72.

Douglas S. Richardson and Jeff W. Lichtman. 2015. Clarifying Tissue Clearing. *Cell* 162, 2 (2015), 246–57. https://doi.org/10.1016/j.cell.2015.06.067

D. Rueckert, L. I. Sonoda, C. Hayes, D. L G Hill, M. O. Leach, and D.J. Hawkes. 1999. Non-rigid registration using free-form deformations: application to breast MR images. *IEEE Trans. Med. Imaging* 18, 8 (1999), 712–21. https://doi.org/10.1109/42.796284

Stephan Saalfeld, Richard Fetter, Albert Cardona, and Pavel Tomancak. 2012. Elastic volume reconstruction from series of ultra-thin microscopy sections. *Nat. Methods* 9, 7 (2012), 717–20. https://doi.org/10.1038/nmeth.2072

Johannes Schindelin, Ignacio Arganda-Carreras, Erwin Frise, Verena Kaynig, Mark Longair, Tobias Pietzsch, Stephan Preibisch, Curtis Rueden, Stephan Saalfeld, Benjamin Schmid, et al. 2012. Fiji: an open-source platform for biological-image analysis. *Nat. Methods* 9, 7 (2012), 676–82. https://doi.org/10.1038/nmeth.2019

Julia A. Schnabel, Daniel Rueckert, Marcel Quist, Jane M. Blackall, Andy D. Castellano-Smith, Thomas Hartkens, Graeme P. Penney, Walter A. Hall, Haiying Liu, et al. 2001. A Generic Framework for Non-rigid Registration Based on Non-uniform Multi-level Free-Form Deformations. In *MICCAI '01*. Springer, 573–81. https://doi.org/10.1007/3-540-45468-3_69

A. Sotiras, C. Davatzikos, and N. Paragios. 2013. Deformable Medical Image Registration: A Survey. *IEEE T. Med. Imaging* 32, 7 (2013), 1153–90. https://doi.org/10.1109/TMI.2013.2265603

Birte Steiniger, Lars Rüttinger, and Peter J. Barth. 2003. The Three-dimensional Structure of Human Splenic White Pulp Compartments. *J. Histochem. Cytochem.* 51, 5 (2003), 655–63. https://doi.org/10.1177/002215540305100511

B. S. Steiniger, S. Bubel, W. Böckler, K. Lampp, A. Seiler, B. Jablonski, M. Guthe, and V. Stachniss. 2013. Immunostaining of Pulpal Nerve Fibre Bundle/Arteriole Associations in Ground Serial Sections of Whole Human Teeth Embedded in Technovit®9100. *Cells Tissues Organs* 198, 1 (2013), 57–65. https://doi.org/10.1159/000351608

Birte S. Steiniger, Anja Seiler, Katrin Lampp, Verena Wilhelmi, and Vitus Stachniss. 2014a. B lymphocyte compartments in the human splenic red pulp: capillary sheaths and periarteriolar regions. *Histochem. Cell Biol.* 141, 5 (2014), 507–18. https://doi.org/10.1007/s00418-013-1172-z

Birte S. Steiniger, Vitus Stachniss, Verena Wilhelmi, Anja Seiler, Katrin Lampp, Andreas Neff, Michael Guthe, and Oleg Lobachev. 2016. Three-dimensional arrangement of human bone marrow microvessels revealed by immunohistology in undecalcified sections. *PLOS ONE* 11, 12 (12 2016), 1–25. https://doi.org/10.1371/journal.pone.0168173

Birte S. Steiniger, Verena Wilhelmi, Anja Seiler, Katrin Lampp, and Vitus Stachniss. 2014b. Heterogeneity of stromal cells in the human splenic white pulp. Fibroblastic reticulum cells, follicular dendritic cells and a third superficial stromal cell type. *Immunol.* 143, 3 (2014), 462–77. https://doi.org/10.1111/imm.12325

D. Sun, S. Roth, and M. J. Black. 2010. Secrets of optical flow estimation and their principles. In *2010 IEEE Computer Society Conference on Computer Vision and Pattern Recognition*. 2432–9. https://doi.org/10.1109/CVPR.2010.5539939

Gabriel Taubin. 1995. A signal processing approach to fair surface design. In *Proceedings of the 22nd annual conference on Computer graphics and interactive techniques*. ACM, 351–8.

P. Thevenaz, T. Blu, and M. Unser. 2000. Interpolation revisited. *IEEE T. Med. Imaging* 19, 7 (2000), 739–58. https://doi.org/10.1109/42.875199

J.-P. Thirion. 1998. Image matching as a diffusion process: an analogy with Maxwell's demons. *Med. Image Anal.* 2, 3 (1998), 243–60. https://doi.org/10.1016/S1361-8415(98)80022-4

Christine Ulrich, Oleg Lobachev, Birte S. Steiniger, and Michael Guthe. 2014. Imaging the Vascular Network of the Human Spleen from Immunostained Serial Sections. In *Visual Computing for Biology and Medicine (VCBM '14)*, Ivan Viola, Katja Buehler, and Timo Ropinski (Eds.). EG. https://doi.org/10.2312/vcbm.20141185

Tao Wan, B. Nicolas Bloch, Shabbar Danish, and Anant Madabhushi. 2013. A novel point-based nonrigid image registration scheme based on learning optimal landmark configurations. In *Medical Imaging 2013: Image Processing (Proc. SPIE 8669)*. 866934–866934–12. https://doi.org/10.1117/12.2007153

Yiwen Xu, J. Geoffrey Pickering, Zengxuan Nong, Eli Gibson, John-Michael Arpino, Hao Yin, and Aaron D. Ward. 2015. A Method for 3D Histopathology Reconstruction Supporting Mouse Microvasculature Analysis. *PLoS ONE* 10, 5 (05 2015), 1–24. https://doi.org/10.1371/journal.pone.0126817

C. W. Zitnick, N. Jojic, and Sing Bing Kang. 2005. Consistent segmentation for optical flow estimation. In *International Conference on Computer Vision (ICCV '05)*. IEEE, 1308–15. https://doi.org/10.1109/ICCV.2005.61